A Radar Simulator for High-Resolution Nonhydrostatic Models

OLIVIER CAUMONT,* VÉRONIQUE DUCROCQ,* GUY DELRIEU,+ MARIELLE GOSSET,+ JEAN-PIERRE PINTY,# JACQUES PARENT DU CHÂTELET,@ HERVÉ ANDRIEU,& YVON LEMAÎTRE,** AND GEORGES SCIALOM**

* *CNRM/Game (Météo-France, CNRS), Météo-France, Toulouse, France*
+ *LTHE, Grenoble, France*
# *Laboratoire d'Aérologie, Toulouse, France*
@ *DSO, Météo-France, Trappes, France*
& *LCPC, Bouguenais, France*
** *CETP, Vélizy, France*

(Manuscript received 30 May 2005, in final form 21 January 2006)

ABSTRACT

A full radar simulator for high-resolution (1–5 km) nonhydrostatic models has been developed within the research nonhydrostatic mesoscale atmospheric (Meso-NH) model. This simulator is made up of building blocks, each of which describes a particular physical process (scattering, beam bending, etc.). For each of these blocks, several formulations have been implemented. For instance, the radar simulator offers the possibility to choose among Rayleigh, Rayleigh–Gans, Mie, or T-matrix scattering methods, and beam bending can be derived from an effective earth radius or can depend on the vertical gradient of the refractive index of air. Moreover, the radar simulator is fully consistent with the microphysical parameterizations used by the atmospheric numerical model.

Sensitivity experiments were carried out using different configurations for the simulator. They permitted the specification of an observation operator for assimilation of radar reflectivities by high-resolution nonhydrostatic numerical weather prediction systems, as well as for their validation. A study of the flash flood of 8–9 September 2002 in southeastern France, which was well documented with volumetric data from an S-band radar, serves to illustrate the capabilities of the radar simulator as a validation tool for a mesoscale model.

1. Introduction

Currently, operational numerical weather prediction (NWP) systems consist of global atmospheric models, which run typically at horizontal resolutions ranging from 20 to 50 km and mesoscale limited area models with approximately 10-km grid meshes. A significant evolution in NWP systems is planned in upcoming years. It is envisaged that the current operational models will be replaced or complemented by a new atmospheric model generation, which will be nonhydrostatic with horizontal resolutions of 1–3 km. Almost all Eumetnet[1] Short-Range Numerical Weather Prediction (SRNWP) consortia [High Resolution Limited Area Model (HIRLAM), Consortium for Small Scale Modelling (COSMO), Aire Limitée Adaptation Dynamique Développement International (ALADIN), ALADIN-Limited Area Modelling in Central Europe (LACE), and the Met Office (MO)] envisage such developments. For instance, Météo-France's next operational NWP model, called Application of Research to Operations at Mesoscale (AROME), is planned to be operational by 2008. It is being designed to run at a resolution of only a few kilometers. The National Center for Atmospheric Research (NCAR), the National Oceanic and Atmospheric Administration (NOAA), the Center for Analysis and Prediction of Storms (CAPS), and a number of scientists at universities are also working to-

Corresponding author address: Dr. Olivier Caumont, CNRM/GMME/Micado, Météo-France, 42, avenue Gaspard Coriolis, 31 057 Toulouse CEDEX 1, France.
E-mail: olivier.caumont@meteo.fr

[1] This network is dedicated to the organization of cooperative programs between its 21 European members.

gether on the Weather Research and Forecasting (WRF) model, which is intended to supersede existing models from all these institutions (see information online at http://www.wrf-model.org/).

Because of limited computational resources, moist convection has to be parameterized in current operational models. This subgrid parameterization has inherent limitations that contribute to the low confidence of quantitative precipitation forecasts (QPFs) in current operational models (e.g., Fritsch and Carbone 2004). For the future generation of high-resolution NWP models, a significant improvement of the representation of clouds and precipitation is expected, both by explicit treatment of moist convection and advanced parameterization of microphysical processes. Such improvements have already been demonstrated in some case studies using nonhydrostatic research models like the nonhydrostatic mesoscale atmospheric (Meso-NH) model (Ducrocq et al. 2002; Richard et al. 2003) or the fifth-generation Pennsylvania State University (PSU)–NCAR Mesoscale Model (MM5) (Trier et al. 2004). These studies have also shown the necessity to improve data assimilation systems, focusing on the use of higher-resolution observations such as either mesonet in situ observations, or high-resolution remote sensing information like Meteosat Second Generation (MSG) radiances or radar data. Indeed, ground-based radar data have the advantage of having a high spatial and temporal resolution, covering large areas (sometimes at different elevations), and being produced on a routine basis with increasing quality in many countries (Gekat et al. 2004). This has motivated the use of radar data by some national weather services (NWSs) to improve the quality of operational analyses and forecasts.

A scheme that directly assimilates reflectivities first requires an observation operator, which mainly acts as a radar simulator for the forward model. Many radar simulators are available in the literature, but they often only focus on a few specific points. Some of them concentrate on microphysical aspects and attempt to establish relationships with their associated errors between radar measurements and the hydrometeor contents of the sounded atmosphere. For instance, Vivekanandan et al. (1993) tried to link polarimetric measurements to mixtures of different types of hydrometeors. Others favored hydrological aspects; Giuli et al. (1994), Anagnostou and Krajewski (1997), or Capsoni et al. (2001) more or less attempted to quantify measurement errors in rain-rate estimations by carrying out sensitivity tests in order to better link reflectivity fields to rain rates. The goal of Pellarin et al. (2002) was to better quantify rain rates in mountainous areas. Boudevillain and Andrieu (2003) tried to estimate the accuracy of vertically integrated liquid water contents retrieved by radar measurements. Some attempts were made to assimilate radar data in high-resolution models, but they often included Doppler velocities only (Lindskog et al. 2004). When reflectivities are also assimilated, the corresponding observation operator is always very basic (Wu et al. 2000; Xiao et al. 2004). It is worth noting that Haase and Crewell (2000) have developed a complete radar reflectivity simulator, the Radar Simulation Model (RSM), which uses predicted precipitation and cloud fields of the nonhydrostatic mesoscale German Lokal-Modell (LM). Only a limited number of sensitivity tests have been carried out by Haase and Crewell (2000) in order to model beam bending and attenuation by air and hydrometeors. It is proposed here that sensitivity tests be made more systematically for each component of the radar simulator. In addition to the formulation of attenuation and beam bending, the sensitivity to beam broadening, scattering theory, and drop size distribution is also investigated. For that, a modular simulator is developed with a variety of possibilities for each module. Then, the various options are evaluated in order to specify the level of sophistication needed for the radar simulator. In the evaluation, the two following applications of the radar simulator are considered: the radar simulator can be used both as a validation tool for high-resolution forecasts and also as an observation operator for a variational assimilation system.

The radar simulator is developed inside the research nonhydrostatic high-resolution Meso-NH model, the characteristics of which are close to those planned for future NWP systems. The simulator will be flexible enough to be able to emulate X-, C-, or S-band radars that operate at different elevations in either research or operational modes. In this study, the sensitivity tests focus more on Météo-France's operational radars. By 2006, Météo-France's operational network, named Aramis, will be composed of eight C-band and 16 S-band radars, some of which will be volumetric.

The main purpose of this paper is to describe the radar simulator itself and to outline the results of the sensitivity experiments in order to recommend how to build an observation operator for reflectivity assimilation, as well as how to configure the radar simulator for validation purposes. This latter application is then illustrated on high-resolution forecasts of an extreme flash-flood event.

The radar simulator is described in section 2. It comprises several modules related to respective physical processes such as the beam shape and geometrical extension, and the electromagnetic interactions with hy-

drometeors. The various options that were implemented in Meso-NH are presented for each module. Section 3 describes the case and the meteorological model that serve as a basis for simulations of radar reflectivities. In section 4, sensitivity experiments for each radar simulator module are carried out for the selected case, and outcomes for specifying the simulator as a validation tool for high-resolution model forecast or as an observation operator for data assimilation systems are discussed. Finally, section 5 proposes an illustration of the radar simulator used as a validation tool for the 8–9 September 2002 extreme flash-flood event.

2. Radar simulator

Conventional weather radars (i.e., neither polarimetric nor Doppler) are considered here. Such radars work as follows: the radar antenna emits a horizontally polarized electromagnetic pulse. The antenna's geometry, which is an axisymmetrical paraboloid, is designed such that the emitted energy is mostly confined into a narrow conical beam. When this radiation hits a target, a part of the energy is absorbed and the rest of the energy is scattered in all directions. In particular, some energy is backscattered in the direction of the radar, and measured by the antenna in reception mode. The amplitude of the backscattered signal depends on the nature, shape, and size of the scatterer. The range to target is computed by measuring the lag between the emission and the reception of the pulse, insofar as air is considered as nondispersive.

The equation that is used to compute reflectivities is first recalled. As shown hereafter, this equation can be split into subexpressions that correspond to particular physical processes. These subexpressions are evaluated in independent modules that are then described.

a. General expression for equivalent reflectivity factors

The radar equation that relates the power P_t (W) that is emitted by the radar with that received (P_r; W) can be written without much loss of generality in spherical coordinates as (see, e.g., Doviak and Zrnić 1993, p. 73)

$$P_r(\mathbf{r}_0) = \frac{P_t g^2 \lambda^2}{(4\pi)^3} \int_0^{2\pi} \int_0^{\pi} \int_0^{cT_s/2} \frac{\eta(\mathbf{r}) l(\mathbf{r})^2}{r^4} f^4(\theta,\phi) |W(r_0 - r)|^2 r^2 \sin\theta \, dr \, d\theta \, d\phi, \quad (1)$$

where r, ϕ, and θ are the radial, azimuth, and zenith coordinates, respectively; $\mathbf{r_0}$ is the vector of length r_0 (m) that links the radar emitting antenna to the center of the resolution volume, that is, the part of space that contributes most to the returned power; g is the gain in emission of the antenna, which normally includes attenuation by radome and waveguide; c designates the speed of light in vacuo (m s^{-1}); T_s (s) is the pulse-repetition time; λ (m) is the wavelength of the emitted signal; $\mathbf{r}$ (m) is the vector that links the antenna to the current point; f^2 is the antenna's radiation pattern; W is the range-weighting function; η (m^{-1}) is the radar reflectivity, which is defined by

$$\eta(\mathbf{r}) \doteq \frac{1}{\delta\mathcal{V}} \sum_{i \in \delta\mathcal{V}} \sigma_i = \sum_{j \in \text{type}} \int_0^{\infty} \sigma_j(D, \mathbf{r}) N_j(D, \mathbf{r}) \, dD, \quad (2)$$

where σ_i (m^2) is the backscattering cross section of the ith scatterer located in the infinitesimal volume $\delta\mathcal{V}$ (m^3), $\sigma_j(D, \mathbf{r})$ (m^2) is the backscattering cross section of the particles of diameter D (m) for the precipitating hydrometeor type j, and N_j (m^{-4}) is the hydrometeor size distribution; and l is the total one-path attenuation

$$l(\mathbf{r}) = \exp\left[-\int_0^r \sum_{j \in \text{type}} \int_0^{\infty} C_{ej}(D, \mathbf{r}) N_j(D, \mathbf{r}) \, dD dr \right], \quad (3)$$

where C_{ej} is the extinction cross section of the jth scatterer.

Radar meteorologists use a quantity called equivalent reflectivity factor (Z_e; dBZ, often referred to as "radar reflectivity"), which is related to the measured power by

$$Z_e(\mathbf{r_0}) = 10 \log\left(\frac{r_0^2 P_r(\mathbf{r_0})/C}{1 \text{mm}^6 \text{m}^{-3}} \right), \quad (4)$$

where C is the radar constant

$$C = \frac{P_t g^2 \pi^3 c\tau (\Delta\theta)^2 |K_w|^2}{1024 \lambda^2 \ln 2}, \quad (5)$$

where τ is the pulse duration (s), and $\Delta\theta$ is the 3-dB beamwidth for one-way transmission (rad). The dielectric factor of water $|K_w|^2$ is defined by

$$|K_w|^2 = \left| \frac{m_w^2 - 1}{m_w^2 + 2} \right|^2, \quad (6)$$

where m_w is analogous to the complex refractive index of water; $|K_w|^2$ is approximately 0.93.

Combining Eqs. (1), (4), and (5) yields

$$Z_e(\mathbf{r_0}) = 10\log\left(\frac{10^{18}r_0^2}{1\text{m}^3}\frac{16\lambda^4\ln 2}{\pi^6 c\tau(\Delta\theta)^2|K_w|^2}\int_0^{2\pi}\int_0^{\pi}\int_0^{cT_s/2}\frac{\eta(\mathbf{r})l(\mathbf{r})^2}{r^2}f^4(\theta,\phi)|W(r_0-r)|^2\sin\theta\, dr\, d\theta\, d\phi\right), \quad (7)$$

which is the basic equation from which one can simulate equivalent reflectivity factors.

When the following assumptions are made

- the scatterers are composed of liquid water,
- the Rayleigh approximation is valid for these scatterers,
- attenuation is negligible,
- the receiver's bandwidth is infinite, and
- the antenna's radiation pattern complies with the work by Probert-Jones (1962),

Eq. (7) reduces to

$$Z_e(\mathbf{r_0}) = 10\log\left(\frac{1}{1\text{ mm}^6\text{m}^{-3}}\int_0^{\infty}D^6N_r(D,\mathbf{r_0})\,dD\right). \quad (8)$$

In the following, for each process involved in Eq. (7), several options have been implemented in the radar simulator.

b. Beam shape

To correctly simulate the process of measuring, one has to know the sampling volume. This resolution volume is radially determined by the sampling process and orthoradially defined by the antenna's radiation pattern.

Radar measurements consist in sampling return echoes at regular times. Because the gate length is about one order smaller than the model's horizontal resolution (typically, gate lengths are of about 250 m, and the model resolution is greater than 1 km), it is not expected that effects related to the finite receiver bandwidth (Doviak and Zrnić 1993) will lead to significant errors. Therefore, the gate length is set to $c\tau/2$, and it is assumed that the range to the target is large compared to the gate length and that all scatterers located in this gate equally contribute to the received signal.

In this case,

$$W(r_0-r) = \begin{cases} 1 & \text{if } r \in \left(\left[r_0-\frac{c\tau}{4}, r_0+\frac{c\tau}{4}\right]\right), \\ 0 & \text{otherwise,} \end{cases} \quad (9)$$

and Eq. (7) reads

$$Z_e(\mathbf{r_0}) = 10\log\left(\frac{10^{18}r_0^2}{1\text{m}^3}\frac{16\lambda^4\ln 2}{\pi^6 c\tau(\Delta\theta)^2|K_w|^2}\int_0^{2\pi}\int_0^{\pi}\eta(r_0,\theta,\phi)\right)l(r_0,\theta,\phi)^2 f^4(\theta,\phi)\sin\theta\, d\theta\, d\phi\int_0^{cT_s/2}\frac{|W(r_0-r)|^2}{r^2}dr, \quad (10)$$

$$= 10\log\left(\frac{10^{18}}{1\text{m}^3}\frac{8\lambda^4\ln 2}{\pi^6(\Delta\theta)^2|K_w|^2}\int_0^{2\pi}\int_0^{\pi}\eta(r_0,\theta,\phi)l(r_0,\theta,\phi)^2 f^4(\theta,\phi)\sin\theta\, d\theta\, d\phi\right). \quad (11)$$

The power density pattern of the antenna results from diffraction. For recent radars as well as for the French network radars, sidelobe power is at least 20 dB smaller than the maximum power of the main lobe. Sidelobes are therefore neglected in the simulator, whereas various possibilities have been introduced to represent the main lobe.

A common way of modeling the main lobe is to represent it as a Gaussian function. Thus, Probert-Jones (1962) derived an expression for reflectivities that assumed that the antenna's radiation pattern was a Gaussian function and that the sounded atmosphere was homogeneous in each range gate, bounded at 3 dB. This model is available in our simulator to represent the main lobe, but a more refined model was also implemented that takes into account variations of reflectivities within resolution volumes because when reflectivities undergo a strong spatial gradient, the local value of reflectivity needs to be taken into account when integrating the power density pattern over the antenna aperture. Otherwise, beam broadening can lead to serious underestimations, as pointed out by Germann and Joss (2004). Indeed, whereas horizontal gradients of synthetic reflectivities remain smooth because the model mesh size is at least on the order of the gate size, in the vertical, the model resolution can be much finer than the gate extension (approximately several tens of meters for the models in the low levels, in comparison

to several hundreds for the gate). So it may seem natural to integrate the product of the antenna directivity function and the local reflectivity value.

In Eq. (11), the following integral is evaluated:

$$I = \int_0^{2\pi} \int_0^{\pi} f^4(\theta, \phi) H(r_0, \theta, \phi) \sin\theta \, d\theta \, d\phi, \quad (12)$$

where H stands for ηl^2. Following Probert-Jones (1962), I can be approximated by

$$I = \int_{-\infty}^{\infty} \int_{-\infty}^{\infty} e^{-8 \ln 2 \frac{\theta^2}{\Delta\theta^2}} e^{-8 \ln 2 \frac{\phi^2}{\Delta\theta^2}} H(r_0, \theta, \phi) \, d\theta \, d\phi. \quad (13)$$

In our simulator, I is evaluated by means of Gauss–Hermite or Gauss–Legendre quadrature (Press et al. 1986). These methods take advantage of the particular form of the integrand to perform efficient calculations.

Note that using a single abscissa in Gauss–Hermite quadrature yields the same results as those initially proposed by Probert-Jones (1962)—a constant directivity function within a cone of revolution, multiplied by a corrective factor. With this method, it is unrealistic to take more than about three points because the integration interval spans over too large an interval. Therefore, the Gauss–Hermite quadrature cannot match the model resolution where it is high. With the Gauss–Legendre quadrature, the integration interval is fixed; it was set to the −3 dB level angle. All points used by this quadrature method lie within this interval, and increasing their number results in increasing the accuracy of the quadrature method. The number of points can thus be adapted to match the model resolution locally. Conversely, this method needs several abscissas to get a good convergence, so it is consequently ill suited to low-resolution quadratures.

For the French radar network, the gate reflectivities are projected on a cone-shaped Cartesian grid of 1 km × 1 km resolution and 560 km × 560 km size; reflectivity for each pixel is obtained by averaging gate reflectivities that are located inside the corresponding area. The radar simulator samples azimuths so that at least one gate reflectivity is allocated to each pixel of the Cartesian grid.

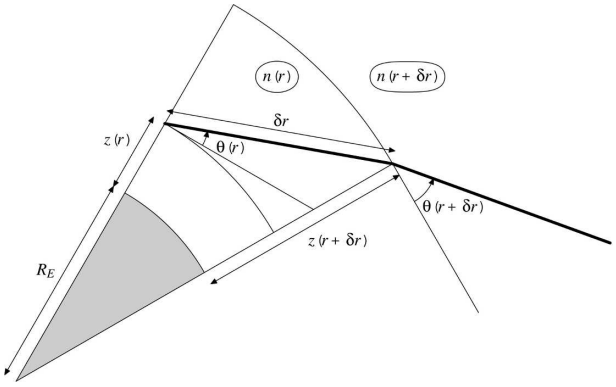

FIG. 1. Refraction of the radar ray for an infinitesimal layer of the atmosphere.

c. Beam bending

Two methods have been implemented to take beam bending into account. Indeed, as a radar beam travels through the atmosphere, it encounters various refractive indexes. This variation is responsible for the bending of the electromagnetic beam according to Snell's law. At radio frequencies, the refractive index n is mainly influenced by the water vapor partial pressure (e), total pressure (p), and temperature (T). From experimental datasets, Smith and Weintraub (1953) give the widely used relationship

$$N = \frac{77.6}{T}\left(p + 4810\frac{e}{T}\right), \quad (14)$$

where $N = (n - 1) \times 10^6$ is the refractivity, p and e are in hectopascals, and T is in kelvins. The radar simulator offers the possibility to compute the path of the radar ray using the following formulas (with the notations of Fig. 1):

$$z(r + \delta r) = \{[R_E + z(r)]^2 + \delta r^2 + 2\delta r[R_E + z(r)] \sin\theta(r)\}^{1/2} - R_E, \quad (15)$$

$$\theta(r + \delta r) = \pm \arccos\left(\frac{R_E + z(r)}{R_E + z(r + \delta r)} \frac{n(r)}{n(r + \delta r)} \cos\theta(r)\right), \quad (16)$$

where z is the altitude (m MSL), R_E is the earth radius (m), θ is the elevation, and δr is a small increment along the beam path (m). Equation (16) is derived from Snell's law for a spherical geometry [e.g., Bean and Dutton 1968, their Eq. (3.68)].

This method, hereafter called GRADN, is computationally expensive and necessitates passing information from one gate to the next one on the same path. It requires a good knowledge of the state of the atmosphere, particularly at low levels. It can be observed

TABLE 1. Size distribution parameters according to Meso-NH microphysical parameterization; ρ_w is the density of liquid water, and $\Gamma: z \mapsto \int_0^\infty t^{z-1}e^{-t}dt$ is the gamma function. See the text for other notation.

Type	$g(D)$	α	β	C	X	$G(\beta)$
Rainwater	$\Lambda \exp(-\Lambda D)$	$\pi\rho_w/6$	3	8×10^6	-1	$\Gamma(1 + \beta)$
Snow/aggregate	$\Lambda \exp(-\Lambda D)$	0.02	1.9	5	1	$\Gamma(1 + \beta)$
Graupel	$\Lambda \exp(-\Lambda D)$	19.6	2.8	5×10^5	-0.5	$\Gamma(1 + \beta)$
Primary ice	$\frac{3}{2}\Lambda^9 D^8 \exp[-(\Lambda D)^3]$	0.82	2.5	Concentration	0	$\frac{1}{2}\Gamma[3 + (\beta/3)]$

that for most situations, using an effective earth radius (Schelleng et al. 1933) is acceptable. This method, called hereafter EFRAD, is the second method that has been implemented in the radar simulator to compute the beam path. In this case, assuming an earth slightly larger than the real one, the propagation path is considered as a straight line. This actually corresponds to an idealized atmosphere, which enables straightforward analytical computation of each radar gate height. This idealized atmosphere model simply states that the vertical gradient of the refractive index is equal to $-1/(4R_E)$. In this case, the effective earth radius is 4/3 larger than the real one. In a few situations, the actual vertical gradient of the refractive index will substantially differ from $-1/(4R_E)$. Such situations occur, for example, for clear sky during the night, leading to a temperature inversion and a quick decrease of humidity with altitude, or when warm, dry air flows over cooler water and is cooled and humidified in the lower layers, or also in storm outflows (e.g., Battan 1973). The issue is critical when the vertical gradient is lower than the standard value at low elevations, which can cause the beam to hit the ground.

d. Backscattering and attenuation

Backscattering and attenuation are involved in the computation of equivalent reflectivity factors. They appear in Eqs. (2) and (3). These equations require the knowledge of hydrometeor size distributions. These distributions are defined using the microphysical scheme of Meso-NH (Caniaux et al. 1994; Pinty and Jabouille 1998) and are expressed as generalized gamma distributions multiplied by the total number concentration N_0 [$N(D) = N_0 g(D)$]. Table 1 presents the size distributions for Meso-NH hydrometeor types (rainwater, graupel, snow, and primary ice). The generalized gamma distributions reduce to exponential distributions for rain, graupel, and snow. The slope parameter Λ is related to the total number concentration by $N_0 = C\Lambda^X$. Using a mass–diameter relationship [$m(D) = \alpha D^\beta$] to express the mass of each hydrometeor, the hydrometeor content M can be expressed as

$$M = \int_0^\infty m(D)N(D)\,dD = \alpha C \Lambda^{X-\beta} G(\beta), \quad (17)$$

where $G(\beta)$ is given in Table 1.

Graupel is considered as a fully wetted hydrometeor below the melting level; above it, it is a mixture of ice and air. Snow and primary ice categories are considered as mixtures of ice and air, and snowflakes are converted into graupel when falling through the melting level.

A number of methods are available from the literature to compute the backscattering and extinction cross sections. They range from simple methods (e.g., Rayleigh) to very accurate ones that take into account the shapes of the scatterers (e.g., volumetric methods). The Rayleigh approximation is valid when the size parameter (which is defined as $x = \pi D/\lambda$) is sufficiently small. Whereas for S band this approximation can be considered valid, it may not be the case for C- or X-band radars. Therefore, it is useful to compare results with more accurate methods. The Mie (or Lorenz–Mie) method consists of explicitly solving Maxwell's equations for an isotropic homogeneous sphere of any size. The Rayleigh theory can be extended to spheroids, which are modeled as anisotropic spheres. In the following, this theory is referred to as the Rayleigh–Gans theory after the works by Rayleigh (1897) and Gans (1912). In the simulator, two axis ratio functions (ratio of minor to major axis) are implemented. The first is a modified version of the experimental results of Pruppacher and Beard (1970),

$$\frac{a}{b} = \begin{cases} 1.03 - 62D_e & \text{for} \quad D_e \geq 0.5 \text{ mm}, \\ 1 & \text{for} \quad D_e < 0.5 \text{ mm}, \end{cases} \quad (18)$$

where D_e (m) is the equivolumetric diameter of the raindrop, a is the vertical axis, and b is the horizontal axis. The second one is (Andsager et al. 1999)

$$\frac{a}{b} = \begin{cases} 1.012 - 14.4D_e - 1.03 \times 10^4 D_e^2 & \text{for} \quad D_e \in [1.1 \text{ mm}; 4.4 \text{ mm}], \\ 1.0048 + 0.57D_e - 2.628 \times 10^4 D_e^2 & \text{elsewhere} \quad \text{(Beard and Chuang 1987)}, \\ \quad + 3.682 \times 10^6 D_e^3 - 1.677 \times 10^8 D_e^4 . & \end{cases} \quad (19)$$

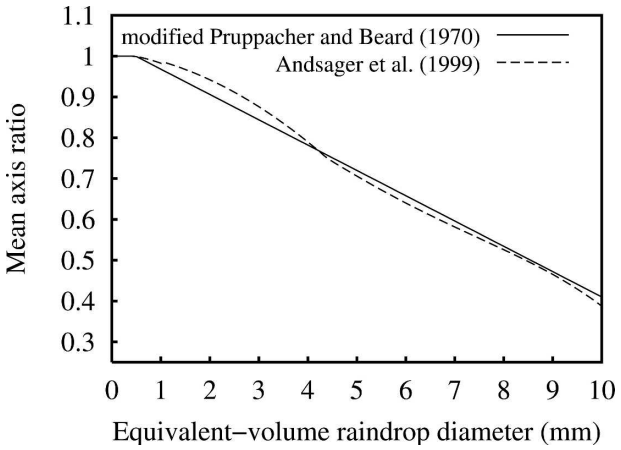

FIG. 2. Axis ratios as functions of equivalent-volume drop diameters D_e (mm).

Figure 2 shows the axis ratios as functions of D_e for both of these approximations.

The T-matrix method can be viewed as a further refinement of the previous method, which is valid for any body size and shape, but it is easier to implement for bodies of revolution (e.g., spheroids). The T-matrix method enables the study of the influence of oblateness and size parameter on the simulated reflectivity. All four of these methods (Rayleigh, Mie, Rayleigh–Gans, and T matrix) are implemented in the radar simulator. The implementation of the Mie method uses the algorithm of Bohren and Huffman (1983), while the T-matrix method uses a modified version of the code presented by Mishchenko and Travis (1998).

Scattering methods need a dielectric function, also called permittivity, to characterize the electrical properties of scatterers. For pure water particles, the dielectric function is taken from Liebe et al. (1991), while the model of Hufford (1991) is taken for pure ice. It is not straightforward to model scattering associated with hydrometeors containing ice. Two problems arise. The microphysical scheme used by the NWP model only considers three classes of ice hydrometeors, which cannot accurately represent the continuous variety of ice particles encountered in observed cloudy systems. Moreover, even if the microphysical scheme was able to handle more-refined classes, the scattering of each hydrometeor species would not be straightforward; these species have complex shapes and are mixtures of ice, water, and air, which interact in a complex way with electromagnetic waves. Here, the following assumptions are made: for particles made of ice and air only (snow, primary ice, and graupel above the melting level), the diameter is the one of a sphere made of pure ice that would have the same mass (e.g., Smith 1984). For water-coated graupel, which is made of ice, water, and air, the diameter is the one of an equivalent-mass sphere made of 14% water and 86% ice as spheroidal inclusions (following Rasmussen et al. 1984). The corresponding dielectric function is then computed following Bohren and Battan (1982).

Attenuation, or extinction, is the result of scattering and absorption. In the atmosphere it is mainly caused by large particles like large raindrops. Thus, extinction by air is often supposed to be a small constant. Relying on the work of Van Vleck (1947a,b), Bean and Dutton (1968) assessed a specific attenuation at $8\ 10^{-3}$ dB km^{-1} for the C band and at $2\ 10^{-3}$ dB km^{-1} for the S band. Attenuation by gases is neglected in our study. Attenuation by hydrometeors is directly computed, along with backscattering in the simulator; scattering methods provide both σ_j and C_{ej} in Eqs. (2) and (3), respectively. Whereas it does not attain significant values for S band, it is a crucial issue for C band. For instance, Scarchilli et al. (1993) reported that specific attenuation could attain 0.5 dB km^{-1}.

3. Case study

a. Observations

On 8–9 September 2002, a mesoscale convective system (MCS) persisted over the same area in southeastern France. This led to a severe flash flood, which resulted in more than 20 casualties and economic damage amounting to 1.2 billion euros (Huet et al. 2003). Daily accumulated rainfall reached 691 mm in the Gard region. A detailed meteorological and hydrological description of this event is given by Delrieu et al. (2005). The convection developed in the warm sector of a perturbation, well ahead of the surface cold front, which moved slowly eastward. The first convective cells formed early in the morning of 8 September over the Mediterranean Sea. They were advected northeastward while intensifying and merging at the same time. The resulting MCS reached the French Mediterranean coast and became stationary over the Gard region by about 1200 UTC. The convective part of this system regenerated over the Gard region, whereas the stratiform part extended northeastward (Fig. 3a). After 2200 UTC, the system axis pivoted to take on a north–south orientation, and shifted northeastward over the Cévennes-Vivarais mountains (Fig. 3b). Then, it progressively merged with the front that had meanwhile propagated eastward. From 0400 UTC 9 September the frontal perturbation with embedded convection again swept through the Gard region. After 1200 UTC 9 September, the area of active rainfall had left the Gard region.

This event is a good candidate for testing our radar

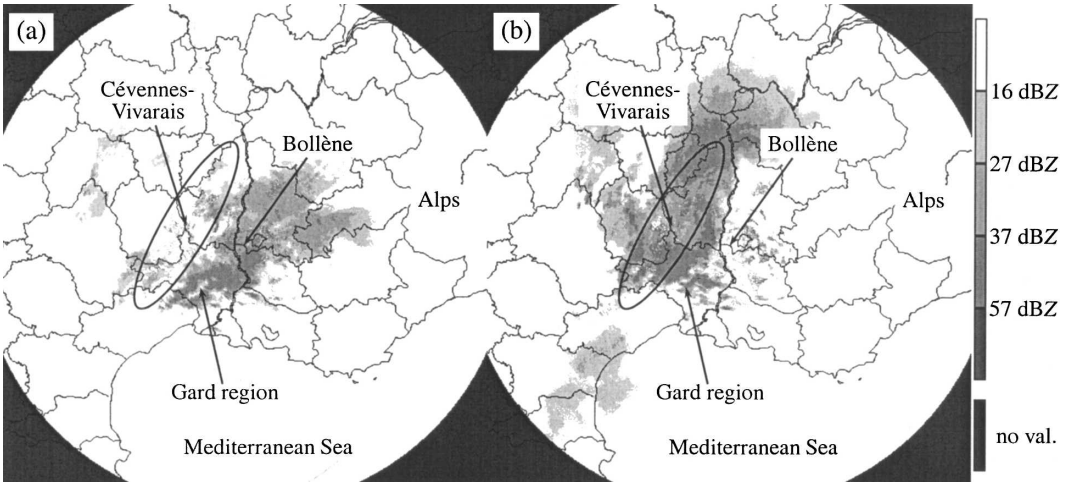

FIG. 3. Observed reflectivities at (a) 1800 UTC 8 Sep 2002 and (b) 0000 UTC 9 Sep 2002 at 1.2° elev from the Bollène S-band radar. Maximum range: 280 km.

simulator because it exhibits both stratiform precipitation and intense convective precipitation. Moreover, during this event, the S-band radar located at Bollène (see Fig. 3a for the location) was operating in an experimental research volumetric mode: 13 different elevations ranging from 0.4° to 18° were sampled every 10 min with a maximum range of 280 km.

b. Meso-NH simulations

The radar simulator has been applied to the outputs at every hour of the Meso-NH model for this case study. Meso-NH is run over two nested grids centered over the region of interest. The horizontal resolution is 9.5 km for the outer grid and 2.4 km for the inner grid, which is close to that used by future NWP systems. Both grids have 40 vertical levels that are unequally spaced from 70 m at lower levels to 900 m at the top. A bulk microphysical scheme (Caniaux et al. 1994; Pinty and Jabouille 1998) governs the equations of the six following water species: vapor, cloud water, liquid water, graupel, snow, and pristine ice. For the outer domain, the subgrid-scale convection is parameterized by the Kain and Fritsch (1993) scheme, adapted to the Meso-NH model by Bechtold et al. (2001), whereas no convective scheme is used for the 2.4-km grid. The radar simulator is applied to the inner domain outputs. The initial state is provided by the mesoscale initialization of Ducrocq et al. (2000), which uses a large-scale Arpege analysis (Météo-France), valid for 1200 UTC 8 September 2002 as a background. This finescale initialization is composed of two steps: the first one consists of a mesoscale surface observation analysis (Calas et al. 2000; Ducrocq et al. 2000), and the second step consists of an adjustment of humidity and hydrometeors based on a preanalysis of the cloudy and rainy areas associated with the developing storm at 1200 UTC 8 September. This preanalysis is derived from radar reflectivities and from the IR Meteosat brightness temperature. Ducrocq et al. (2002) have shown that this finescale initialization may significantly improve the QPF. This is true for the 8–9 September 2002 event (Ducrocq et al. 2004; Chancibault et al. 2006; the mesoscale initialization contributes to the determination of the correct location of the precipitation over the Gard region during the first stage of the event.

4. Simulator configurations for validation and assimilation purposes

Sensitivity tests have been carried out on each simulator module in order to specify configurations that must be appropriate to each usage. Here stress is laid on two particular usages—for data monitoring and design of an observation operator for assimilation purposes. For both usages, the current study considers data from the French radar network composed of S- and C-band radars, which are often used operationally. Thus, a series of experiments was conducted for the 8–9 September 2002 case. The reference, named E0, uses the simplest (and fastest) formulations for each module. The configuration of a new experiment is obtained by upgrading the formulation of one particular module. By comparing the resulting reflectivity fields of this new experiment with those of experiment E0, it is possible to decide whether a basic formulation is sufficiently

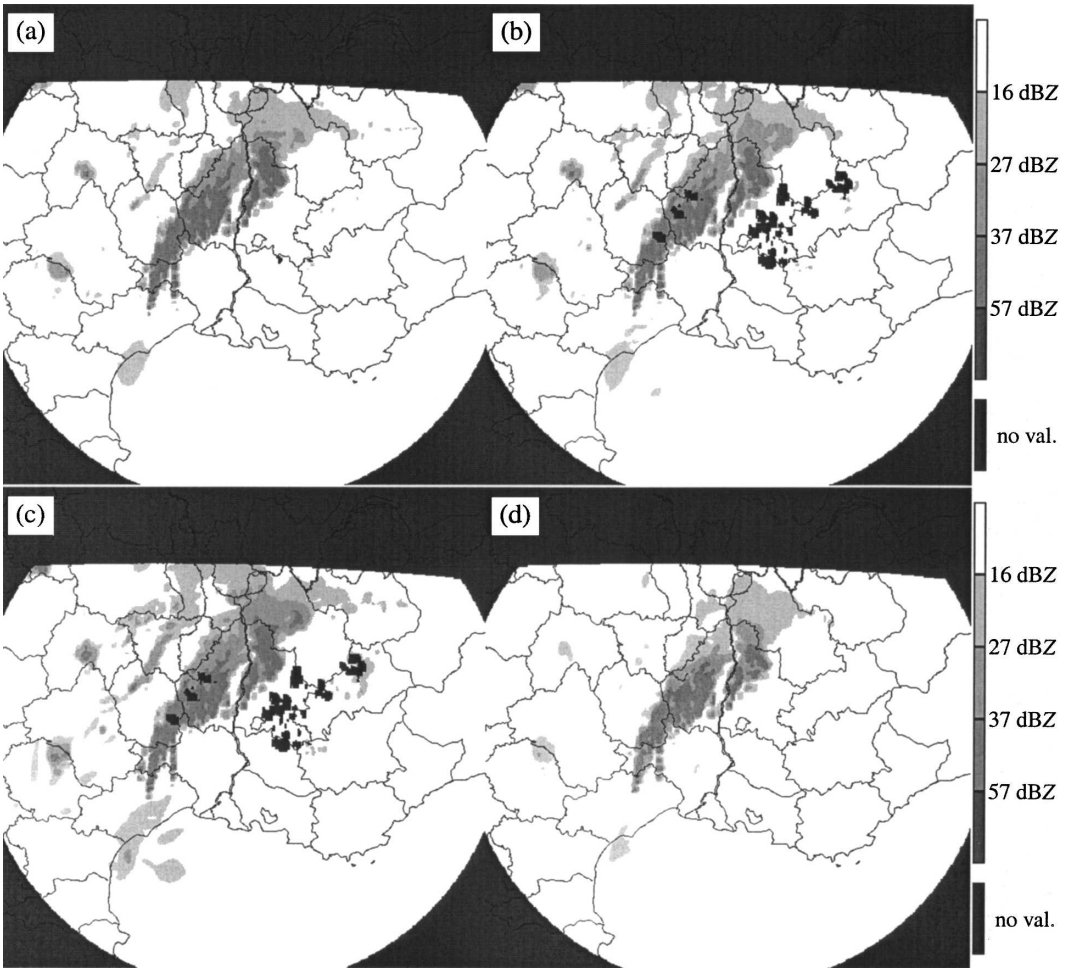

FIG. 4. Reflectivities at 0100 UTC 9 Sep (Bollène radar) from (a) E0, elev 1.2°; (b) E1, elev 1.2°; (c) E0, elev 0.6°; and (d) E0, elev 1.8°. On all simulated data maps, black areas correspond to pixels for which simulated data cannot be computed; i.e., they are out of the Meso-NH domain, they are out of radar range, or they are ground echoes.

accurate or whether an upgraded formulation is necessary.

An example of plan position indicator (PPI) obtained with simulation E0 is given in Fig. 4a for the 1.2° elevation of the Bollène radar at 0100 UTC 9 September 2002; Table 2 summarizes the main results of E0 for all elevations and the whole considered period, and Fig. 5 displays the temporal evolution of the maximum reflectivity for each hydrometeor type. In convective cells, rainwater and graupel produce the highest reflectivities, which correspond to the highest contents for these species.

a. Beam shape

Experiment E1 is intended to assess the effect of a vertical discretization of the beam pattern by a Gauss-

TABLE 2. Maximum simulated reflectivities (Z_{ej} max) for each hydrometeor type (j) and associated hydrometeor contents (M_j), total reflectivity (Z_e), time, and elevation from E0 emulating the Bollène S-band radar between 1600 UTC 8 Sep and 0600 UTC 9 Sep 2002.

Hydrometeor type (j)	Z_{ej} max (dBZ)	M_j (g m^{-3})	Z_e (dBZ)	Time	Elev (°)	Altitude (km MSL)
Rain	56	6.0	57	0300 UTC 9 Sep	1.2	1.6
Pristine ice	28	0.61	33	1800 UTC 8 Sep	9.0	10.0
Snow	40	1.5	41	0500 UTC 9 Sep	6.0	4.0
Graupel	47	4.2	47	1600 UTC 8 Sep	6.0	3.6

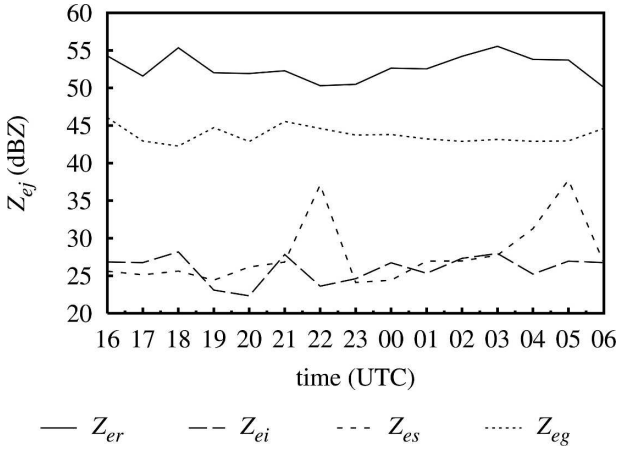

FIG. 5. Evolution of peak reflectivity (Z_e; dBZ) for each hydrometeor type (the *r, i, s,* and *g* subscripts refer to rain, primary ice, snow, and graupel, respectively) between 1600 UTC 8 Sep and 0600 UTC 9 Sep (experiment E0) for all elevations of the Bollène radar.

ian function with three points (see section 2b). Figures 4a and 4b show a comparison between E0 and E1 at 0100 UTC 9 September for an elevation angle of 1.2°. Taking beam broadening into account results in enhancing areas where the beam hits the model orography; this feature can be seen in Fig. 4b (black spots). In terms of the values of the reflectivities, the main differences occur for the farthest gates where the beam is broadened. For instance, one can see that the stratiform region located in the northern part of the domain is underestimated in E0. Figures 4c and 4d display the reflectivities of the lower and upper elevations that are taken into account in E1. Therefore, reflectivities in Fig. 4b correspond somehow to the weighted sum of reflectivities in Figs. 4a, 4c, and 4d. It can be clearly seen that the beam at 1.2° elevation from E0 overshoots the stratiform precipitation located to the northwest of the radar. The 0.6° PPI from E0 enables the consideration of the echoes returned by this area. It is therefore necessary to account for the vertical broadening for both assimilation and validation purposes.

b. Beam bending

In this section, the GRADN and EFRAD methods are compared. Figure 6a shows the difference of gate altitudes computed by both methods. In this figure, the angular sectors of the unavailable pixels are due to the fact that gate heights cannot be computed once the beam hits the ground in E2. This comparison shows that there is a systematic bias between the two methods for the farthest range gates, which increases with range to reach about 350 m at 300 km. This result is consistent with, for example, Bean and Dutton (1968), who state that the gradient of N used in the 4/3 earth radius model is only realistic in low levels of the atmosphere. Figure 6b shows the effect of abnormal propagation on ray paths for a low elevation. The vertical gradient of refractivity computed along a ray path to the north (Fig. 7a) explains why the beam is bent more than usual; in the lower gates, this gradient is much less than the one used in the EFRAD model. This feature is explained by a temperature inversion in the lower atmosphere associated with the cold pool of the storm (see Fig. 7b), which typically entails superrefraction. However, although E2 is superior to E0 in taking into account sub- or superrefraction, it can be noticed that the accuracy of gate heights in E2 strongly relies on the quality of the model refractivity field used. The latter has to be correctly analyzed or predicted and seems to be prone to a large variability. Taking into account local air refrac-

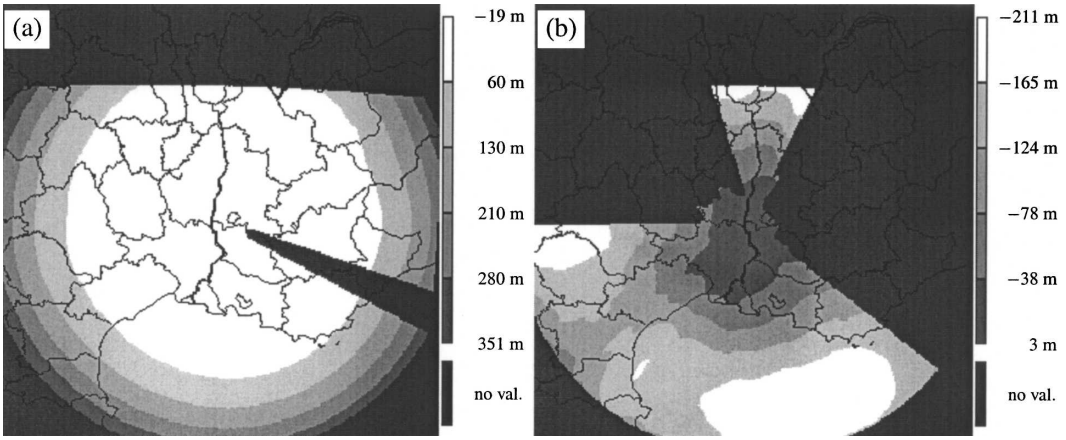

FIG. 6. Difference of gate altitude between E2 and E0: (a) mean value of 1.2° for the whole experiment (between 1600 UTC 8 Sep to 0600 UTC 9 Sep), and (b) at 2300 UTC 8 Sep at 0.4°.

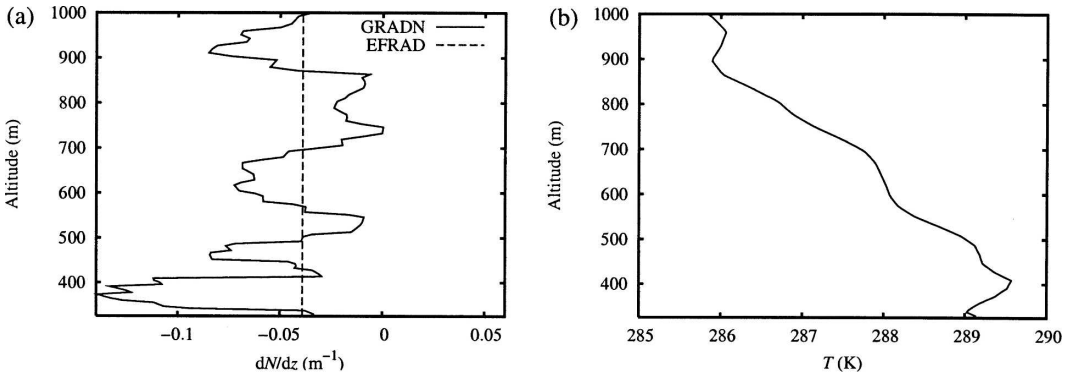

FIG. 7. Altitude of beam gate (m) vs (a) vertical gradient of refractivity (solid line for local Snell's law and dashed line for standard 4/3 earth radius method), and (b) temperature (K) for the GRADN method, respectively, at 2300 UTC 8 Sep, with elev of 0.4° and azimuth 0° (north).

tion index gradients for beam bending could yield no improvement in some cases, and, consequently, it is not desirable to do it for both applications. Moreover, in our case, the assimilation system software uses massive parallelization and treats observations as packets of vertical columns, which does not allow for gate-by-gate computations that are necessary for the beam-bending GRADN method.

c. *Backscattering*

Figure 8 depicts the departures of the equivalent reflectivity factors between one scattering theory and the Rayleigh approximation, which is only valid for small size parameters. Notice that increasing the water content M_r results in shifting the peak of the raindrop size distribution toward large diameters, which increases the contribution of larger raindrops to the overall reflectivity. Approximations used in the different scattering methods depart from each other mainly for large raindrops (i.e., for large size parameters). This feature can be quantitatively assessed in Fig. 8.

Experiment E3, which was performed for the 8–9 September case (Table 3), uses the Mie theory considering C-band radar. It can be seen in Fig. 9a and Table 4 that, for C band and for rain only, the difference between Mie and Rayleigh scattering never exceeds 0.9 dB, while rainwater contents reach 6 g m^{-3}. For ice particles, differences between both methods are negligible (Table 4). Concerning raindrop oblateness, when the T-matrix solution (E5) is compared with that from Mie theory (E3) for our case, the difference between the two solutions can attain +1.8 dB for a rainwater content of about 6 g m^{-3} (Fig. 9b). This difference is, of course, always positive because only horizontal polarization radio wave pulses are transmitted and received, and thus only the horizontal dimension of precipitation particles is measured.

The comparison between experiments E4 and E5

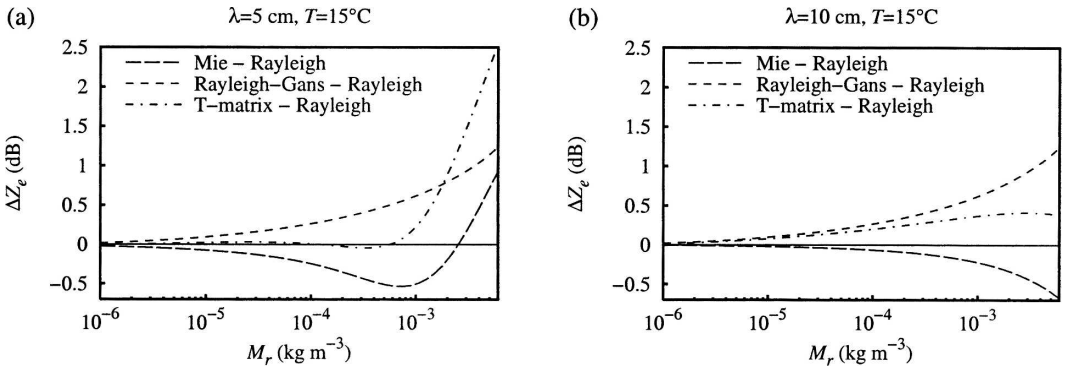

FIG. 8. Departures from Rayleigh scattering by raindrops in terms of equivalent reflectivity factors as functions of rainwater contents (M_r) for (a) $\lambda = 5$ cm and (b) $\lambda = 10$ cm at 15°C. The Rayleigh and Mie solutions are applicable to spheres, whereas the Rayleigh–Gans and T-matrix solutions are computed for spheroids with axis ratios that follow Eq. (18).

TABLE 3. Characteristics of the sensitivity experiments. MPB70 and AND99 stand for axis ratios after Eq. (18) and Eq. (19), respectively.

Expt	Beam bending	Scattering model	Attenuation	Vertical antenna's pattern
E0	EFRAD	Rayleigh	No	Dirac
E1	EFRAD	Rayleigh	No	Three-point Gaussian
E2	GRADN	Rayleigh	No	Dirac
E3	EFRAD	Mie (C band)	No	Dirac
E4	EFRAD	T-matrix (C band, MPB70)	No	Dirac
E5	EFRAD	T-matrix (C band, AND99)	No	Dirac
E6	EFRAD	Rayleigh (third order, C band)	Yes	Dirac
E7	EFRAD	Rayleigh (sixth order, C band)	Yes	Dirac
E8	EFRAD	Mie (C band)	Yes	Dirac
E9	EFRAD	T-matrix (C band, AND99)	Yes	Dirac
E10	EFRAD	Rayleigh (third order, S band)	Yes	Dirac
E11	EFRAD	Rayleigh (sixth order, S band)	Yes	Dirac
E12	EFRAD	Mie (S band)	Yes	Dirac

shows, in accordance with, for example, Gorgucci et al. (2000), that the formulation of the axis ratio function does not notably affect the reflectivities; for both experiments, they do not disagree by more than 0.11 dB (Fig. 10).

Thus, sophisticated scattering theories do not improve reflectivities substantially (even at C band), but conversely increase computational costs. Therefore, the Rayleigh/Mie approximations seem sufficient considering the level of complexity of the microphysical schemes generally used by high-resolution nonhydrostatic models (bulk microphysical parameterization with only three to four precipitating species). More complex scattering models, like the T-matrix model, should be reserved for other applications such as studies on polarimetry.

d. Attenuation

Specific attenuation resulting from hydrometeors can be computed with the scattering models described above for backscattering estimations. Specific attenuations in the Rayleigh approximation and for the Mie, Rayleigh–Gans, and T-matrix methods have been estimated and are shown in Fig. 11 as functions of rainwater content. It is obvious from Fig. 11b that attenuation can be neglected for S band in most cases. It is also clear from Fig. 11 that truncating the expression for specific attenuation under the Rayleigh approximation to terms of order x^3 underestimates the attenuation (only 0.26 against 1.07 dB km^{-1} for water contents above 6 g m^{-3} at $\lambda = 5$ cm). The Rayleigh–Gans approach also provides an expression of attenuation that is limited to the

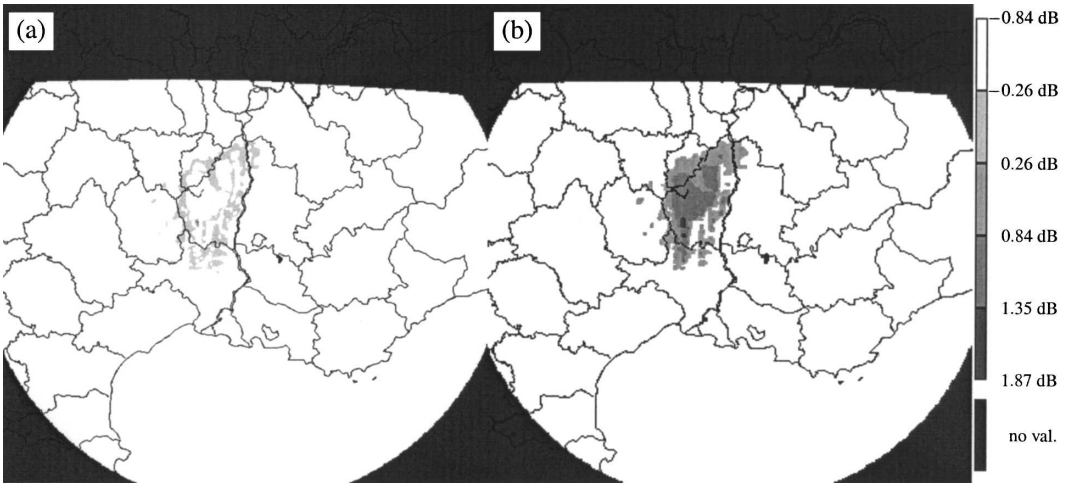

FIG. 9. Reflectivity differences between various backscattering theories at C band for rain only, at 0300 UTC 9 Sep, with 1.2° PPI (i.e., where and when this difference is maximum): (a) Mie–Rayleigh (E3–E0), and (b) T matrix–Mie (E5–E3).

TABLE 4. Maximum simulated reflectivity differences (ΔZ_{ej} max) between E3 and E0 for each hydrometeor type (j) and associated hydrometeor contents (M_j), time, elevation, and altitude between 1600 UTC 8 Sep and 0600 UTC 9 Sep 2002.

Hydrometeor type (j)	ΔZ_{ej} max (dB)	M_j (g m^{-3})	Time	Elev (°)	Altitude (km MSL)
Rain	0.88	6.0	0300 UTC 9 Sep	1.2	1.6
Pristine ice	−0.09	0.09	1600 UTC 8 Sep	6.0	8.7
Snow	−0.10	1.5	0500 UTC 9 Sep	6.0	4.0
Graupel	−0.05	5.5	2100 UTC 8 Sep	9.0	5.5

third order, which explains why its curve is similar to that from the third-order Rayleigh expression. Even if the Rayleigh theory for attenuation up to the sixth order approaches the solution for Mie theory, they are still relatively far from each other at $\lambda = 5$ cm. It is also recognized that raindrop oblateness enhances horizontal specific attenuation. This can be quantified by comparing the T-matrix and the Mie solutions in Fig. 11. Experiments E6–E12 attempt to document the differences between the scattering methods for the 8 September 2002 case. Table 5 shows that, for C and S bands on this case, the Rayleigh approximation largely underestimates specific attenuations by raindrops and therefore cannot be used to assess attenuations. On the contrary, attenuation by graupel is accurately described by the Rayleigh theory. Experiment E8 shows that the specific attenuation by hydrometeors can attain significant values for C band (Table 5), especially for rain and, to a lesser extent, graupel. Indeed, the maximum specific attenuation for this simulated case reaches a value of 2.5 dB km^{-1}, which is mainly due to rain. Modeling rain as oblate spheroids (E9) leads to larger attenuation; specific attenuation by rain reaches 3 dB km^{-1}. As a result, the total attenuation when considering Mie scattering for a C-band radar (E8) reaches the maximum value of 38 dB at 0600 UTC 9 September at an elevation of 1.2° (Fig. 12b); rain contributes up to 24 dB, and graupel up to 14 dB; contributions from other hydrometeor types are negligible.

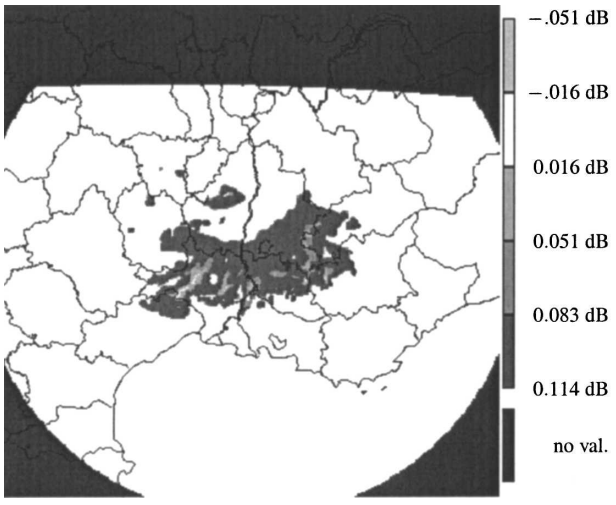

FIG. 10. Reflectivity differences between formulations of axis ratios that follow Eq. (18) and Eq. (19) (E4–E5, at 1800 UTC 8 Sep, elev of 1.2°, in dB).

In summary, the Mie theory should at least be used to model attenuation. This only applies when considering C-band radars; S-band attenuation by precipitation may be considered negligible. However, accounting for attenuation can constitute a strong constraint in the design of observation operators because it needs gate-by-gate computations. It could be better to handle attenuation in the preprocessing of data. In that case, regions beyond high-reflectivity areas on radar images have to be flagged before the assimilation in order to adapt their treatments in the data assimilation step.

5. Application of the radar simulator to the model validation

As stated above, the Meso-NH model succeeds in simulating the quasi-stationary convective system of 8–9 September 2002, with both a convective and a stratiform part. Here it is proposed to illustrate how the radar simulator may be helpful to validate the model forecasts using this simulation. Radar simulations are compared with observations of the Bollène S-band radar. Therefore, the radar simulator can be used with the Rayleigh scattering method and attenuation can be safely neglected. A vertical three-point Gauss–Hermite quadrature is used to take the beam broadening into account. This configuration corresponds to experiment E1.

Figure 13 shows a comparison between the peak value of simulated and observed reflectivities at an elevation of 1.2°. The maximum simulated reflectivities are a bit lower than those observed. This is consistent with the fact that simulated precipitation totals from Meso-NH are lower than those observed (rain gauges). It can also be explained by the remaining observed ground echoes that were not rejected by the clutter removal algorithm for the observed radar reflectivity. The difference in the variability of reflectivities between observations and simulations in Fig. 13 is artificial and comes from the sampling time difference (5 min for observations versus 1 h for simulations).

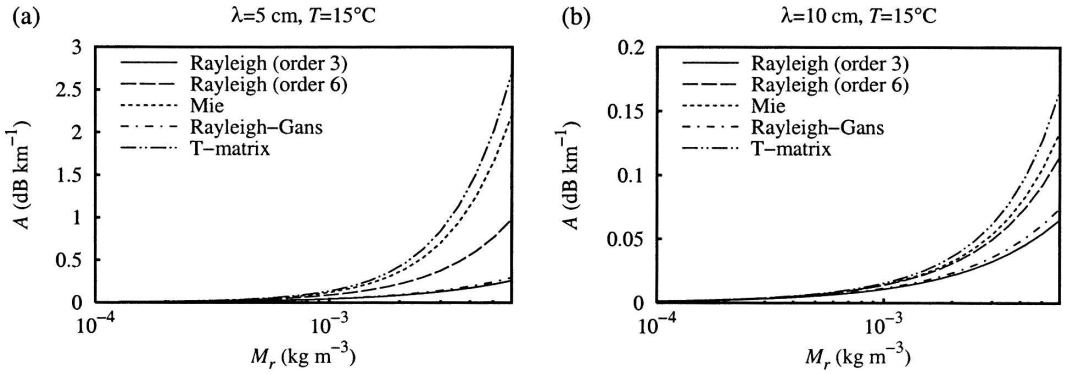

FIG. 11. Two-way specific attenuations by rain (A) as a function of rainwater content (M_r) for (a) $\lambda = 5$ cm and (b) $\lambda = 10$ cm at 15°C. The Rayleigh and Mie solutions apply to spheres, whereas Rayleigh–Gans and T matrix arise from Eq. (18). "Order" corresponds to the last term taken into account when expressing specific attenuation in the Rayleigh approximation as a truncated Maclaurin size parameter series (see, e.g., Bohren and Huffman 1983, p. 135). Note that ordinate axis scales differ in (a) and (b).

Figure 14 represents the area for which reflectivities exceed a particular threshold (30 or 40 dBZ, respectively) for the simulation and the observations. In this figure, one can see that the extension of the convective part, which corresponds to pixels with a reflectivity above 40 dBZ, is approximately the same order of magnitude in the simulation and the observations. In contrast, the model does not catch the growth of the stratiform part from 2000 UTC onward, as evidenced by the jump in the size of the area for which observed reflectivities are above 30 dBZ. This is clearly shown in Fig. 15, which compares observations and modeled reflectivities at 2100 UTC; the stratiform part in the north of the domain (region A in Fig. 15a) is not sufficiently

TABLE 5. Maximum simulated specific two-way attenuations and corresponding contents for the 8–9 Sep 2002 case (Bollène radar) for experiments E6–E12. For E9, pristine ice, snow, and graupel characteristics are the same as in E8.

Expt	Hydrometeor type	Max specific two-way attenuation (dB km^{-1})	Content (g m^{-3})	Elev (°)	Time	Altitude (km MSL)
E6	Rain	0.34	6.2	1.2	1800 UTC 8 Sep	2.7
	Pristine ice	7.5×10^{-5}	0.60	9.0	0600 UTC 9 Sep	8.4
	Snow	1.4×10^{-4}	1.5	6.0	0500 UTC 9 Sep	4.0
	Graupel	1.2	4.2	6.0	1600 UTC 8 Sep	3.6
E7	Rain	1.2	6.2	1.2	1800 UTC 8 Sep	2.7
	Pristine ice	2.5×10^{-4}	0.61	9.0	1800 UTC 8 Sep	10.0
	Snow	2.8×10^{-3}	1.5	6.0	0500 UTC 9 Sep	4.0
	Graupel	1.3	4.2	6.0	1600 UTC 8 Sep	3.6
E8	Rain	2.5	6.0	1.2	0300 UTC 9 Sep	1.6
	Pristine ice	2.5×10^{-4}	0.61	9.0	1800 UTC 8 Sep	10.0
	Snow	3.5×10^{-3}	1.6	6.0	2200 UTC 8 Sep	3.5
	Graupel	1.3	4.2	6.0	1600 UTC 8 Sep	3.6
E9	Rain	3.0	6.0	1.2	0300 UTC 9 Sep	1.6
E10	Rain	8.4×10^{-2}	6.2	1.2	1800 UTC 8 Sep	2.7
	Pristine ice	2.0×10^{-5}	0.60	9.0	0600 UTC 9 Sep	8.4
	Snow	3.6×10^{-5}	1.5	6.0	0500 UTC 9 Sep	4.0
	Graupel	0.32	4.2	6.0	1600 UTC 8 Sep	3.6
E11	Rain	0.15	6.2	1.2	1800 UTC 8 Sep	2.7
	Pristine ice	2.7×10^{-5}	0.61	9.0	1800 UTC 8 Sep	10.0
	Snow	2.0×10^{-4}	1.5	6.0	0500 UTC 9 Sep	4.0
	Graupel	0.33	4.2	6.0	1600 UTC 8 Sep	3.6
E12	Rain	0.18	6.2	1.2	1800 UTC 8 Sep	2.7
	Pristine ice	2.8×10^{-5}	0.61	9.0	1800 UTC 8 Sep	10.0
	Snow	3.6×10^{-4}	1.6	6.0	2200 UTC 8 Sep	3.5
	Graupel	0.33	4.2	6.0	1600 UTC 8 Sep	3.6

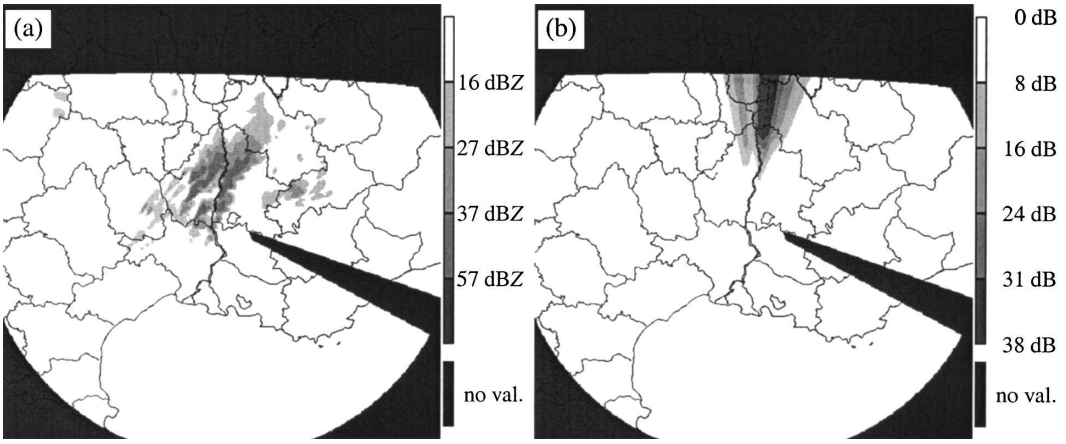

FIG. 12. Total (a) reflectivity (dBZ) and (b) two-way path-integrated attenuation (dB) at 0600 UTC 9 Sep, 1.2° elev (from experiment E8).

developed in the Meso-NH simulation. Nevertheless, Fig. 15 shows that the most active part of the MCS compares quite well in intensity and location with the observations. Vertical extension of the precipitating area also compares well because the maximum altitude where hydrometeors are sufficiently present ($Z_e \geq 8$ dBZ) is about 12 km in both observed radar scans and model (not shown).

The underestimation of the stratiform part might be due to either an underestimation of the ice hydrometeor contents by the model or an inaccurate modeling of the reflectivities of these species by the radar simulator. It is not easy to validate reflectivities for hydrometeors containing ice, because the Meso-NH model discriminates three species while empirical Z–M relationships are estimated for mixtures of these hydrometeors. Moreover, empirical relationships often rely on assumptions that differ from each other (constant density, scattering properties, etc.). Figure 16 displays some Z–M relationships found in the literature along with those computed with Meso-NH parameters for snow and dry graupel. Empirical relationships are scattered because of uncertainties concerning which hydrometeors are really sensed. Different methods are used to establish these relationships, which also contributes to their dispersion. The Meso-NH Z–M relationships for dry graupel compare relatively well with empirical relationships. However, the relationship for snow appears to have a slope that is larger than the Z–M relationships found in the literature. It results that reflectivities seem to be underestimated for snow contents below 0.3 g m^{-3} and overestimated for contents above 0.6 g m^{-3}. Observed reflectivities in region A (Fig. 15a) corre-

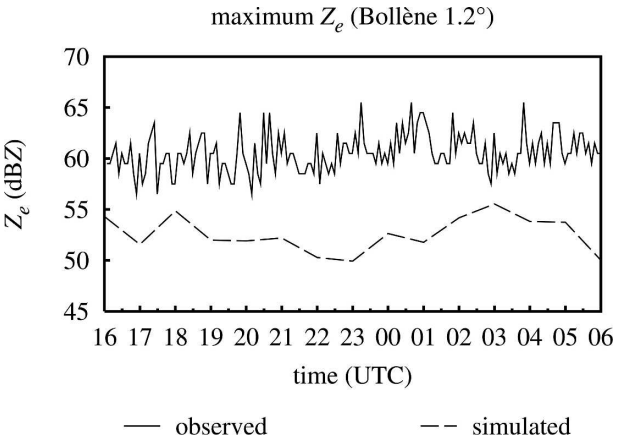

FIG. 13. Simulated (E1) and observed maximum reflectivities (dBZ) between 1600 UTC 8 Sep and 0600 UTC 9 Sep for the Bollène radar, 1.2° elev.

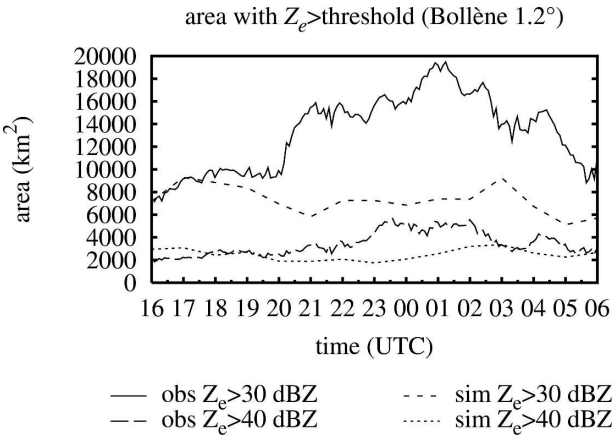

FIG. 14. Simulated (E1) and observed area (km^2) for which the reflectivity is above 30 or 40 dBZ, respectively, between 1600 UTC 8 Sep and 0600 UTC 9 Sep for the Bollène radar, 1.2° elev.

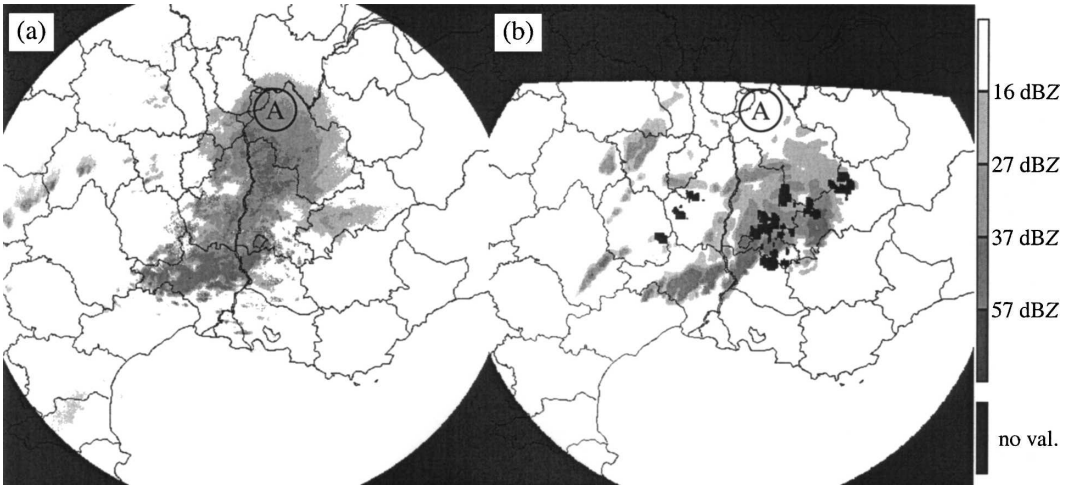

FIG. 15. (a) Observed and (b) simulated reflectivities (dBZ) from the Bollène radar at 2100 UTC 8 Sep 2002 at 1.2° elev.

spond to ice hydrometeor contents in the range from 0.1 to 3 g m^{-3} with respect to the empirical Z–M relationships (Fig. 16). Some reflectivities in this region correspond to ice contents between 0.3 and 0.6 g m^{-3}, where Meso-NH Z–M relationships quite agree with the empirical values. Therefore, this confirms that the underestimation of the stratiform part in region A is due to the Meso-NH model, which fails to produce enough hydrometeors in this region (Fig. 17 confirms this assertion).

6. Summary

A modular simulator of radar reflectivities has been developed inside the postprocessing software of the Meso-NH model. Each module, which represents a particular physical process, received a number of different implementations. Ray paths can be computed in two different manners in the simulator. The first one uses Snell's law at each gate to determine the position of the next gate; the second one assumes that the vertical gra-

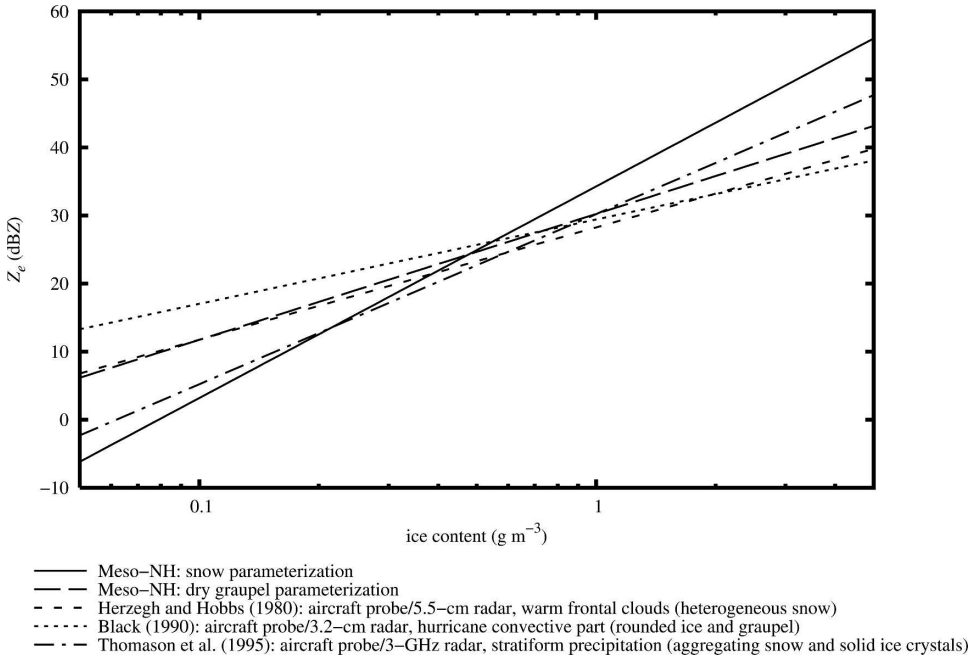

FIG. 16. Z–M relations for snow and dry graupel from the Meso-NH model, and for ice particles from empirical estimations (Z, dBZ; M, g m^{-3}).

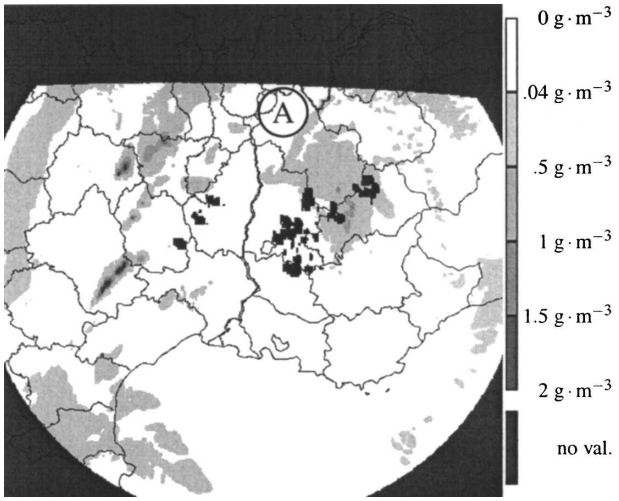

FIG. 17. Sum (g m^{-3}) of simulated snow, graupel, and primary ice contents (E1 at 1.2°) at 2100 UTC 8 Sep.

dient of refractivity is constant. Thus, the trajectory of the beam can be determined analytically. Four scattering methods have been implemented: the Rayleigh theory, its extension to spheroids (denoted by the Rayleigh–Gans theory), the Mie theory, and the T-matrix method. Attenuation can be accounted for; in this case, it is computed according to the selected scattering theory. The vertical and horizontal extension of the beam is accounted for. The resulting reflectivities are computed as weighted averages of Gaussian patterns, using the Gauss–Hermite or Gauss–Legendre method. All of these options differ in their complexity, accuracy, and central processing unit (CPU) time consumption.

Sensitivity tests were performed on each module to determine an adequate configuration to simulate reflectivities from high-resolution NWP systems. At first, the results of the sensitivity experiments clearly show that beam broadening has to be taken into account in the vertical, while it can be neglected in the horizontal as long as the model grid mesh remains above 1 km. Concerning the scattering method, as long as the attenuation is not considered, the Rayleigh method provides sufficient accuracy with respect to the level of complexity of microphysical schemes usually used in NWP systems. However, for C- or X-band radars, attenuation by precipitation cannot be ignored when comparing observed and forecasted reflectivites. It has to be taken into account by the radar simulator, or if that is not possible, by the postprocessing of observed reflectivities by flagging, for example, regions beyond areas with high reflectivities. When the application takes attenuation into account inside the radar simulator, Rayleigh scattering is not suitable for computing attenuation, and Mie scattering has to be used. Concerning the beam bending, it is not obvious that the method using the local vertical gradient of refractivity is superior to the simpler one using the effective earth radius, because this method is strongly related to the quality of the forecast of the thermodynamic parameters. This is particularly crucial in low levels.

The usefulness of the radar simulator for the validation of high-resolution NWP forecasts has been demonstrated for the extreme flash flood of 8–9 September 2002. For that case, which is documented by observations from the Bollène S-band radar, the following configuration was used for the simulator: Rayleigh scattering, no attenuation, standard beam bending, and a three-point vertical Gaussian averaging kernel. Comparison of the simulated and observed reflectivities showed that the location of the simulated storm as well as the intensity of its convective parts are fairly well represented. The simulator helped to show that, however, the NWP model does not correctly simulate the enhancement of the stratiform part of the considered storm from 2000 UTC 8 September 2002 onward.

This radar simulator is also a good framework to implement polarimetric parameters or Doppler radial winds, which will be done in the near future. This study has also helped to configure the observation operator for assimilation of radar reflectivities, which is under development inside the AROME project framework at Météo-France.

Acknowledgments. The authors appreciate the helpful suggestions of the anonymous reviewers. Laurent Labatut is recognized for his technical assistance. The authors also thank Aaron Boone for improving the English of the manuscript.

REFERENCES

Anagnostou, E. N., and W. F. Krajewski, 1997: Simulation of radar reflectivity fields: Algorithm formulation and evaluation. *Water Resour. Res.,* **33,** 1419–1428.

Andsager, K., K. V. Beard, and N. F. Laird, 1999: Laboratory measurements of axis ratios for large raindrops. *J. Atmos. Sci.,* **56,** 2673–2683.

Battan, L. J., 1973: *Radar Observations of the Atmosphere.* University of Chicago Press, 324 pp.

Bean, B. R., and E. J. Dutton, 1968: *Radio Meteorology.* Dover, 435 pp.

Beard, K. V., and C. Chuang, 1987: A new model for the equilibrium shape of raindrops. *J. Atmos. Sci.,* **44,** 1509–1524.

Bechtold, P., É. Bazile, F. Guichard, P. Mascart, and É. Richard, 2001: A mass-flux convection scheme for regional and global models. *Quart. J. Roy. Meteor. Soc.,* **127,** 869–886.

Black, R. A., 1990: Radar reflectivity-ice water content relationships for use above the melting level in hurricanes. *J. Appl. Meteor.,* **29,** 955–961.

Bohren, C. F., and L. J. Battan, 1982: Radar backscattering of

microwaves by spongy ice spheres. *J. Atmos. Sci.,* **39,** 2623–2628.

——, and D. R. Huffman, 1983: *Absorption and Scattering of Light by Small Particles.* John Wiley & Sons, 530 pp.

Boudevillain, B., and H. Andrieu, 2003: Assessment of vertically integrated liquid (VIL) water content radar measurement. *J. Atmos. Oceanic Technol.,* **20,** 807–819.

Calas, C., V. Ducrocq, and S. Sénési, 2000: Mesoscale analyses and diagnostic parameters for deep convection nowcasting. *Meteor. Appl.,* **7,** 143–161.

Caniaux, G., J.-L. Redelsperger, and J.-P. Lafore, 1994: A numerical study of the stratiform region of a fast-moving squall line. *J. Atmos. Sci.,* **51,** 2046–2074.

Capsoni, C., M. D'Amico, and R. Nebuloni, 2001: A multiparameter polarimetric radar simulator. *J. Atmos. Oceanic Technol.,* **18,** 1799–1809.

Chancibault, K., S. Anquetin, V. Ducrocq, and G.-M. Saulnier, 2006: Hydrological evaluation of high-resolution precipitation forecast of the Gard flash-flood event (8–9 September 2002). *Quart. J. Roy. Meteor. Soc.,* in press.

Delrieu, G., and Coauthors, 2005: The catastrophic flash-flood event of 8–9 September 2002 in the Gard region, France: A first case study for the Cévennes-Vivarais Mediterranean Hydrometeorological Observatory. *J. Hydrometeor.,* **6,** 34–52.

Doviak, R. J., and D. S. Zrnić, 1993: *Doppler Radar and Weather Observations.* 2d ed. Academic Press, 562 pp.

Ducrocq, V., J.-P. Lafore, J.-L. Redelsperger, and F. Orain, 2000: Initialization of a fine-scale model for convective-system prediction: A case study. *Quart. J. Roy. Meteor. Soc.,* **126,** 3041–3065.

——, D. Ricard, J.-P. Lafore, and F. Orain, 2002: Storm-scale numerical rainfall prediction for five precipitating events over France: On the importance of the initial humidity field. *Wea. Forecasting,* **17,** 1236–1256.

——, C. Lebeaupin, T. Thouvenin, H. Giordani, K. Chancibault, S. Anquetin, and G.-M. Saulnier, 2004: L'événement des 8–9 Septembre 2002: Situation météorologique et simulation à mésoéchelle (The 8–9 September 2002 extreme flash flood: Meteorological description and mesoscale simulations). *Houille Blanche,* **6,** 86–92.

Fritsch, J. M., and R. E. Carbone, 2004: Improving quantitative precipitation forecasts in the warm season: A USWRP research and development strategy. *Bull. Amer. Meteor. Soc.,* **85,** 955–965.

Gans, R., 1912: Über die Form ultramikroskopischer Goldteilchen. *Ann. Phys.,* **37,** 881–900.

Gekat, F., P. Meischner, K. Friedrich, M. Hagen, J. Koistinen, D. B. Michelson, and A. Huuskonen, 2004: The state of weather radar operations, networks and products. *Weather Radar: Principles and Advanced Applications,* P. Meischner, Ed., Springer, 1–51.

Germann, U., and J. Joss, 2004: Operational measurement of precipitation in mountainous terrain. *Weather Radar: Principles and Advanced Applications,* P. Meischner, Ed., Springer, 52–77.

Giuli, D., L. Baldini, and L. Facheris, 1994: Simulation and modeling of rainfall radar measurements for hydrological applications. *Nat. Hazards,* **9,** 109–122.

Gorgucci, E., G. Scarchilli, V. Chandrasekar, and V. N. Bringi, 2000: Measurement of mean raindrop shape from polarimetric radar observations. *J. Atmos. Sci.,* **57,** 3406–3413.

Haase, G., and S. Crewell, 2000: Simulation of radar reflectivities using a mesoscale weather forecast model. *Water Resour. Res.,* **38,** 2221–2231.

Herzegh, P. H., and P. V. Hobbs, 1980: The mesoscale and microscale structure and organization of clouds and precipitation in midlatitude cyclones. II: Warm-frontal clouds. *J. Atmos. Sci.,* **37,** 597–611.

Huet, P., X. Martin, J.-L. Prime, P. Foin, C. Laurain, and P. Cannard, 2003: Retour d'expérience des crues de Septembre 2002 dans les départements du Gard, de l'Hérault, du Vaucluse, des Bouches-du-Rhône, de l'Ardèche et de la Drôme (Learning from the September 2002 floods in the Gard, Hérault, Vaucluse, Bouches-du-Rhône, Ardèche, and Drôme departments). Rapport de l'Inspection Générale de l'Environnement, Ministère de l'Écologie et du Développement Durable, 133 pp. [Available online at http://www.ecologie.gouv.fr/ IMG/pdf/crues_gard.pdf.]

Hufford, G. A., 1991: A model for the complex permittivity of ice at frequencies below 1 THz. *Int. J. Infrared Millimeter Waves,* **12,** 677–682.

Kain, J. S., and J. M. Fritsch, 1993: Convective parameterization for mesoscale models: The Kain-Fritsch scheme. *The Representation of Cumulus Convection in Numerical Models, Meteor. Monogr.,* No. 46, Amer. Meteor. Soc., 165–170.

Liebe, H. J., G. A. Hufford, and T. Manabe, 1991: A model for the complex permittivity of water at frequencies below 1 THz. *Int. J. Infrared Millimeter Waves,* **12,** 659–674.

Lindskog, M., K. Salonen, H. Järvinen, and D. B. Michelson, 2004: Doppler radar wind data assimilation with HIRLAM 3DVAR. *Mon. Wea. Rev.,* **132,** 1081–1092.

Mishchenko, M. I., and L. D. Travis, 1998: Capabilities and limitations of a current FORTRAN implementation of the T-matrix method for randomly oriented, rotationally symmetric scattered. *J. Quant. Spectrosc. Radiat. Transfer,* **60,** 309–324.

Pellarin, T., G. Delrieu, G.-M. Saulnier, H. Andrieu, B. Vignal, and J.-D. Creutin, 2002: Hydrologic visibility of weather radar systems operating in mountainous regions: Case study for the Ardèche catchment (France). *J. Hydrometeor.,* **3,** 539–555.

Pinty, J.-P., and P. Jabouille, 1998: A mixed-phase cloud parameterization for use in a mesoscale non-hydrostatic model: Simulations of a squall line of orographic precipitation. Preprints, *Conf. on Cloud Physics,* Everett, WA, Amer. Meteor. Soc., 217–220.

Press, W. H., B. P. Flannery, S. A. Teukolsky, and W. T. Vetterling, 1986: *Numerical Recipes: The Art of Scientific Computing.* Cambridge University Press, 818 pp.

Probert-Jones, J. R., 1962: The radar equation in meteorology. *Quart. J. Roy. Meteor. Soc.,* **88,** 485–495.

Pruppacher, H. R., and K. V. Beard, 1970: A wind tunnel investigation of the internal circulation and shape of water drops falling at terminal velocity in air. *Quart. J. Roy. Meteor. Soc.,* **96,** 247–256.

Rasmussen, R. M., V. Levizzani, and H. R. Pruppacher, 1984: A wind tunnel and theoritical study of the melting behavior of atmospheric ice particles. III. Experiment and theory for spherical ice particles of radius 500 μm. *J. Atmos. Sci.,* **41,** 381–388.

Rayleigh, J. W. S., Lord, 1897: On the incidence of aerial and electric waves upon small obstacles in the form of ellipsoids or elliptic cylinders, and on the passage of electric waves through a circular aperture in a conducting screen. *Philos. Mag.,* **44,** 28–52.

Richard, É., S. Cosma, P. Tabary, J.-P. Pinty, and M. Hagen, 2003:

High-resolution numerical simulations of the convective system observed in the Lago Maggiore area on the 17 September 1999 (Map IOP2a). *Quart. J. Roy. Meteor. Soc.,* **129,** 543–564.

Scarchilli, G., E. Gorgucci, V. Chandrasekar, and T. A. Seliga, 1993: Rainfall estimation using polarimetric techniques at C-band frequencies. *J. Appl. Meteor.,* **32,** 1150–1159.

Schelleng, J. C., C. R. Burrows, and E. B. Ferrell, 1933: Ultra-short-wave propagation. *Proc. IRE,* **21,** 427–463.

Smith, E. K., Jr., and S. Weintraub, 1953: The constants in the equation for atmospheric refractive index at radio frequencies. *Proc. IRE,* **41,** 1035–1037.

Smith, P. L., 1984: Equivalent radar reflectivity factors for snow and ice particles. *J. Climate Appl. Meteor.,* **23,** 1258–1260.

Thomason, J. W. G., A. J. Illingworth, and V. Marécal, 1995: Density and size distribution of aggregating snow particles inferred from coincident aircraft and radar observations. *Proc. 27th Conf. on Radar Meteorology,* Vail, CO, Amer. Meteor. Soc., 509–511.

Trier, S. B., E. Chen, and K. W. Manning, 2004: A study of convection initiation in a mesoscale model using high-resolution land surface initial conditions. *Mon. Wea. Rev.,* **132,** 2954–2976.

Van Vleck, J. H., 1947a: Absorption of microwaves by oxygen. *Phys. Rev.,* **71,** 413–424.

——, 1947b: The absorption of microwaves by uncondensed water vapor. *Phys. Rev.,* **71,** 425–433.

Vivekanandan, J., R. Raghavan, and V. N. Bringi, 1993: Polarimetric radar modeling of mixtures of precipitation particles. *IEEE Trans. Geosci. Remote Sens.,* **31,** 1017–1030.

Wu, B., J. Verlinde, and J. Sun, 2000: Dynamical and microphysical retrievals from Doppler radar observations of a deep convective cloud. *J. Atmos. Sci.,* **57,** 262–283.

Xiao, Q., Y.-H. Kuo, J. Sun, W.-C. Lee, D. M. Barker, and E. Lim, 2004: Assimilation of Doppler radar observations and its impacts on forecasting of the landfalling typhoon Rusa (2002). *Proc. Third European Conf. on Radar in Meteorology and Hydrology (Erad3),* Visby, Sweden, Copernicus GmbH, 178–182.